Broad Electronic Modulation of 2D Metal-Organic Frameworks Over Four Distinct Redox States

Lei Wang, ¹Arup Sarkar, ¹ Garrett L. Grocke, ² Daniel William Laorenza, ³ Baorui Cheng, ¹ Andrew Ritchhart, ¹ Alexander S. Filatov, ¹ Shrayesh N. Patel, ² Laura Gagliardi, ^{1,2,4} and John S. Anderson* ¹

¹Department of Chemistry, University of Chicago, Chicago, Illinois 60637, United States

KEYWORDS: 2D MOF, redox tuning, conductivity, switching

ABSTRACT: Two-dimensional (2D) inorganic materials have emerged as exciting platforms for (opto) electronic, thermoelectric, magnetic, and energy storage applications. However, electronic redox tuning of these materials can be difficult. Instead, 2D metal-organic frameworks (MOFs) offer the possibility of electronic tuning through stoichiometric redox changes, with several examples featuring one to two redox events per formula unit. Here we demonstrate that this principle can be extended over a far greater span with the isolation of four discrete redox states in the 2D MOFs $\text{Li}_x\text{Fe}_3(\text{THT})_2$ (x = 0–3, THT = triphenylene hexathiol). This redox modulation results in 10,000-fold greater conductivity, p- to n-type carrier switching, and modulation of antiferromagnetic coupling. Physical characterization suggests that changes in carrier density drive these trends with relatively constant charge transport activation energies and mobilities. This series illustrates that 2D MOFs are uniquely redox flexible, making them an ideal materials platform for tunable and switchable applications.

Introduction

Two-dimensional (2D) inorganic materials have attracted significant interest for their unusual electronic structures and properties. The discovery of graphene in 2004 is exemplary, but many other families of 2D materials have also generated interest for their electronic, optoelectronic, and magnetic applications. In particular, 2D conductive MOFs have emerged as a new class of inorganic-organic hybrid materials with novel electronic and magnetic properties. These materials exhibit the structural rigidity, chemical tunability, and porosity typical of traditional insulating MOFs, but also exhibit electrical conductivity and tunable electronic structures that promise applications in optoelectronics, thermoelectrics, magnetism, and energy storage.

Discrete redox tuning is a unique feature of 2D MOFs that can influence conductivity by modulating redox-hopping as well as band-like charge transport pathways.⁵ Redox changes can occur spontaneously during synthesis or rationally through post-synthetic modification.⁶ There are several examples where discrete 1-2 electron redox changes have switched or modified properties in MOF materials, ^{6a-6c} but their synthetic tunability and porosity suggests that even greater redox-flexibility should be possible with appropriate metal and linker combinations.⁷

Triphenylene-based linkers with ortho-disubstituted donor atoms (N, O and S) feature prominently in redox-active 2D MOFs.⁸ Triphenylenehexathiol (THT) specifically features dithiolene units that are known to be redox-active, offering the possibility of multiple discrete redox-states. Several THT based MOFs have been reported

with high conductivity, charge mobility, and metallic character, but investigations of stoichiometric redox modulation are lacking. We have therefore designed a stannylated triphenylenehexathiolate precursor SnTHT (2,3,6,7,10,11-hexa(bis-dibutyltintyltriphenylene) which enables the bulk synthesis of a crystalline 2D semiconducting Fe MOF, Fe₄(THT)₂, through solvothermal synthesis. The chemical and electronic structure of Fe₄(THT)₂ can be systematically altered through cation exchange and stoichiometric redox manipulation over four distinct redox states (Figure 1A). The electrical, thermoelectric, and magnetic properties of these 2D MOFs are redox tunable, with little to no structural change. Characterization suggests that charge transport is primarily gated by changing carrier densities with only small changes in mobilities and band gaps. These findings illustrate that conducting 2D MOFs are highly modular platforms for extensive redox modulation of physical properties.

Results and Discussion

Synthesis, Structure, and Composition

The stannylated precursor **SnTHT** was obtained similarly to a protected benzene hexathiolate by capping an in-situ generated anionic triphenylenehexathiolate (THT) salt with dialkyl tin groups. ¹⁰ Mixing **SnTHT** with excess FeCl₂ and thiophenol results in smooth transmetalation to form **Fe**₄(**THT**)₂ (Figure S3). The crystallinity of **Fe**₄(**THT**)₂ can be further tuned with differentially substituted thiophenols, suggesting a modulating role for thiophenol in analogy with modulators in other MOF syntheses (Figures S5 and S6). ¹¹ We

²Pritzker School of Molecular Engineering, University of Chicago, Chicago, Illinois 60637, United States

³Department of Chemistry, Massachusetts Institute of Technology, Cambridge, Massachusetts 02139, United States

⁴James Franck Institute, University of Chicago, Chicago, Illinois 60637, United States

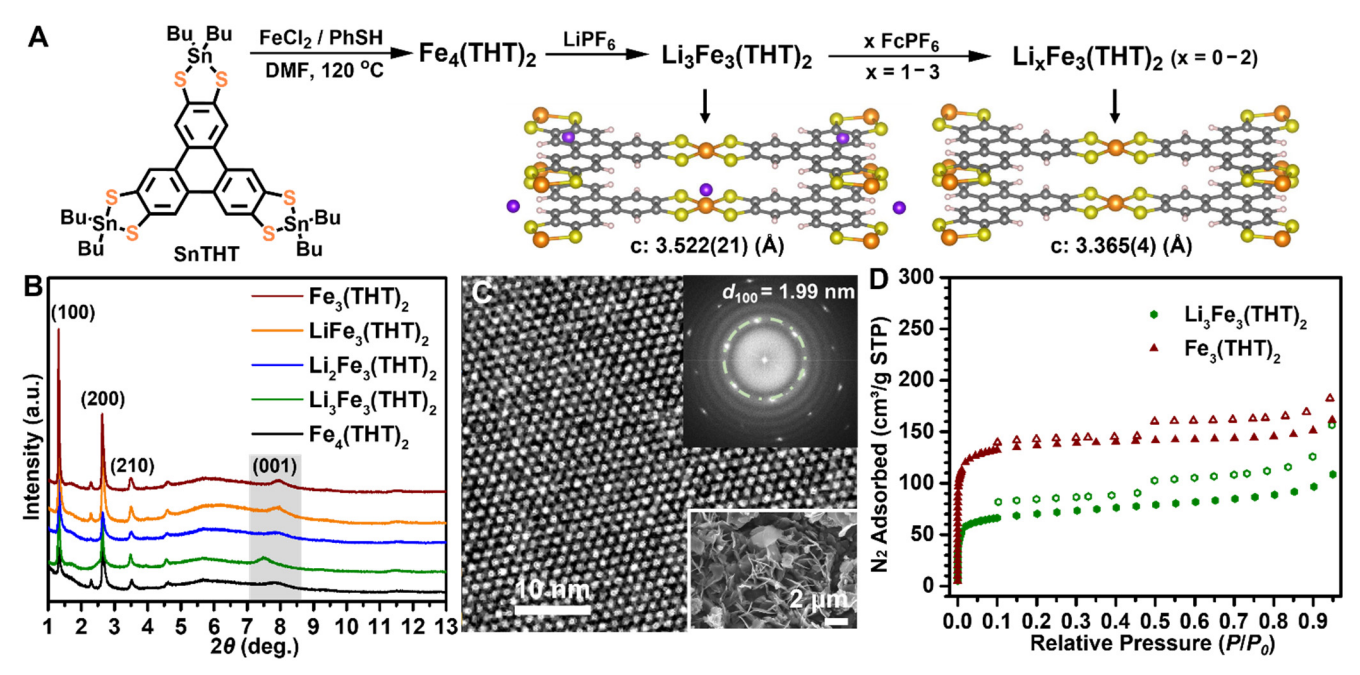


Figure 1. (A) Synthetic scheme for $Fe_4(THT)_2$, and $Li_xFe_3(THT)_2$ (x= 3-0) through cation exchange and stoichiometric oxidation. Structural models of $Li_3Fe_3(THT)_2$ and $Fe_3(THT)_2$ showing different interlayer distances through Rietveld analysis. Color code: orange, Fe; yellow, S; grey, C; purple, Li; pink, H. (B) Comparison of the synchrotron powder X-ray diffraction data (λ = 0.458095 Å for $Li_3Fe_3(THT)_2$ and 0.458963 Å for the others; indices are labeled in the brackets based on a hexagonal space group and the (001) peaks are highlighted in grey box). (C) High-resolution TEM image of the 2D hexagonal structure of $Fe_4(THT)_2$; inset: the fast Fourier transform (top) and SEM image (bottom) showing the flake-like morphology. (D) N_2 adsorption isotherms collected at 77 K for $Li_3Fe_3(THT)_2$ and $Fe_3(THT)_2$. The closed and open symbols are adsorption and desorption data, respectively.

hypothesize that thiophenol modulates spontaneous redox chemistry as we have observed in other semiconducting MOFs (see information for more discussion).6d chromatography shows the production of hydrogen in syntheses of Fe₄(THT)₂ which supports this hypothesis (Figure S4). This finding also indicates redox changes for Fe or THT during the formation of Fe₄(THT)₂ that are further discussed below. Synchrotron powder X-ray diffraction (PXRD) data of Fe₄(THT)₂ are very similar to that observed in the previously reported Fe₃(THT)₂(NH₄)₃9c and FeTHT^{9d} thin film materials, indicative of a similar hexagonal structure with an AA stacking pattern (Figure 1B). Le Bail fitting confirms the hexagonal space group with a lattice parameter of a = b = 22.752(4) Å and c = 3.383(2) Å (Table S1, Figure S10a, see SI for detailed discussion). Scanning electron microscopy (SEM) images show a flake- or sheet-like morphology similar to related 2D stacked frameworks and suggest preferred crystallographic direction along [100] in the material (Figures 1C bottom inset, S16). This observation is consistent with the predominant (100) and (200) peaks in the PXRD data. Highresolution transmission electron microscopy (HRTEM) images also support a hexagonal structure with crystalline domains of 100's of nanometers (Figures 1C and S17a). The fast Fourier transform (FFT) of the HRTEM image further reveals a hexagonal lattice with a d(100) spacing of 1.99 nm and d (200) spacing of 0.97 nm (Figure 1C inset, S17b). All these microscopy results are consistent with the analysis of the PXRD data (Table S2).

Inductively coupled plasma optical emission spectroscopy (ICPOES) and X-ray fluorescence spectroscopy (XRF) both show a Fe:S ratio of ~1:3, higher than the expected ratio for a framework of

Fe₃THT₂ (1:4, Tables S3,S4). This suggests additional charge balancing Fe centers similar to the ammonium ions in Fe₃(THT)₂(NH₄)₃;^{9c} we therefore investigated cation exchanges. Soaking Fe₄(THT)₂ with lithium hexafluorophosphate preserves crystallinity but a shift of the (001) peak to a smaller angle suggests an increased interlayer spacing from 3.383 (2) Å to 3.531(1) Å (Figures 1A, B and S10). Composition analysis shows a 1:4 Fe:S and a 1:1 Fe:Li ratio for an overall formula of Li₃Fe₃(THT)₂. These results indicate an additional Fe(III) counter cation per formula unit in the as-synthesized material that can be replaced by three Li ions upon cation exchange. Li₃Fe₃(THT)₂ has an expanded interlayer distance (~0.15 Å) that can reasonably be attributed to the increased number of cations as well as a slightly larger ionic radius for Li(I) (76 pm) compared to Fe(III) (55-65 pm).

The presence of Fe(III) cations, along with the putative role of thiophenol modulator, also prompted us to investigate postsynthetic redox modification of these materials. Reduction of Li₃Fe₃(THT)₂ with cobaltocene or lithium naphthalenide degrades crystallinity but oxidation is more tractable (Figures S8 and S9). The PXRD peaks of Li₃Fe₃(THT)₂ are maintained even with excess ferrocenium hexafluorophosphate, and the (001) peak in the PXRD data shifts to a larger angle indicating a contraction in the interlayer distance back to ~3.36 Å from Rietveld refinement analysis (Figures S11-S13). Composition analysis reveals a constant 1:4 Fe:S ratio but a decreasing Fe:Li ratio upon oxidation in Li_xFe₃(THT)₂ (Tables S3, S4), suggesting a stoichiometric lithium extraction per oxidation (Figure S3). SEM, HRTEM imaging, and N2 uptake experiments confirm the morphology, symmetry, and porosity of the materials are preserved after post-synthetic cation exchange or stoichiometric oxidation (Figures 1D and S16–S21). The $\,N_2$ adsorption isotherms can be assigned as type I isotherms (microporous). A slightly lower

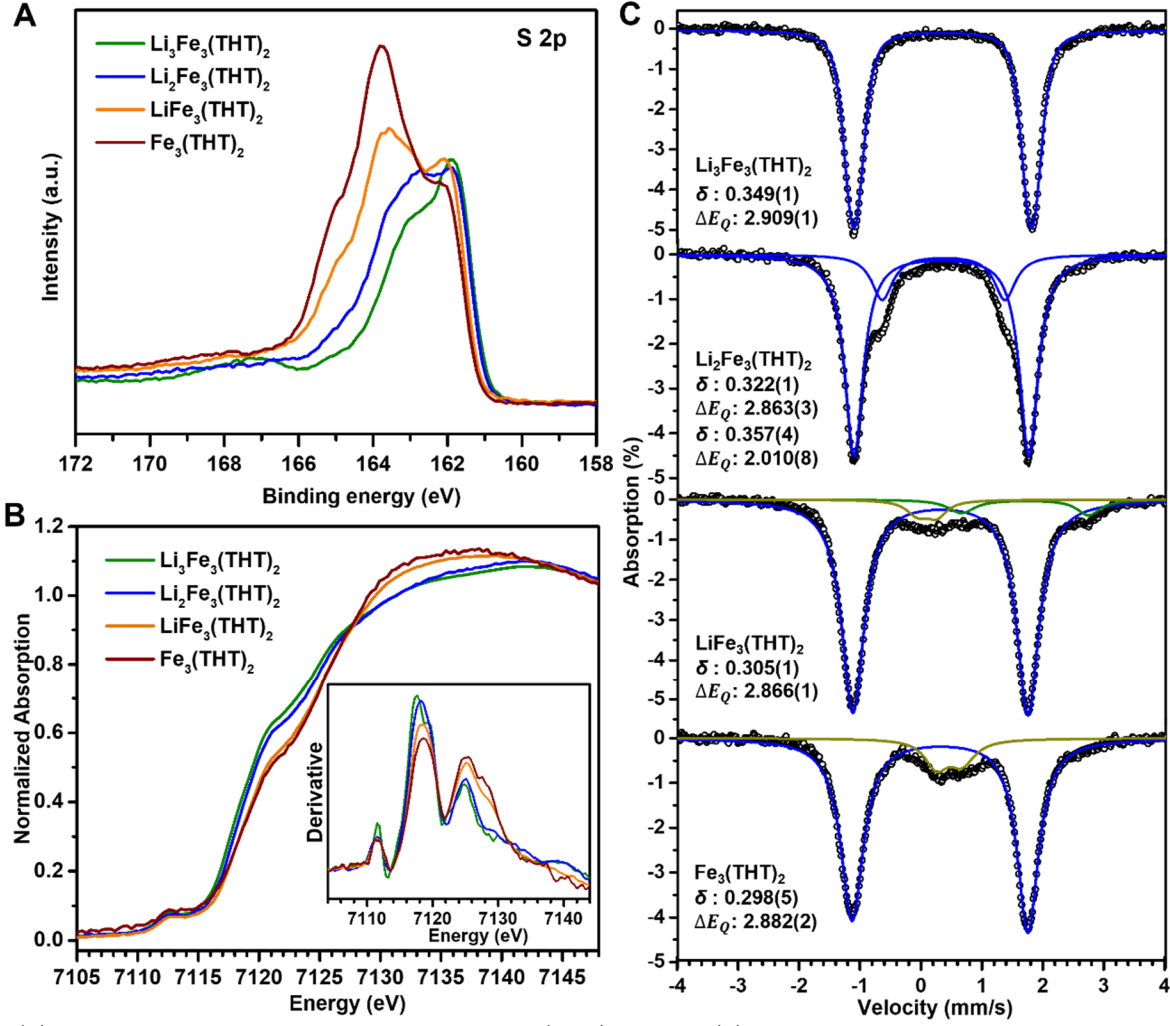


Figure 2. (A) High-resolution S 2p XPS results for the redox Li_xFe₃(THT)₂ materials. (B) Fe K-edge X-ray absorption data with concomitant first derivatives (inset). (C) ⁵⁷Fe Mössbauer spectra recorded at 77 K and fitting results (black dots: experimental data; black solid line: global fitting; blue solid line: Fe(III) species in the material; green and yellow lines: minor impurity or defect Fe centers).

Brunauer–Emmett–Teller (BET) surface area is observed in $\text{Li}_3\text{Fe}_3(\text{THT})_2$ (232.0 m²/g) but is higher in $\text{Fe}_3(\text{THT})_2$ (441.9 m²/g). The increasing porosity along this series is consistent with removal of charge balancing countercations from the pores of the material.

Component Redox-States

As mentioned above, the redox-active components in these materials likely change their oxidation state due to spontaneous redox chemistry during synthesis as well as in post-synthetic manipulations. Several spectroscopic techniques were therefore utilized to study the oxidation state of both metal nodes and organic linkers in these materials. X-ray photoelectron spectroscopy (XPS) shows no general change in the Fe 2p peaks in Li_xFe₃(THT)₂, but a gradual shift towards higher energy in the range of 162 eV to 166 eV for the S 2p peaks (Figures 2A and S24). This observation suggests linker-centered oxidation. This conclusion is supported by Raman spectroscopy; a clear 10 cm⁻¹ shift towards lower energy for the aromatic ring vibrations is observed between SnTHT and the Li_xFe₃(THT)₂ materials consistent with triphenylene backbone bond weakening upon oxidation (Figure S26). The Fe K-edge X-ray absorption near edge structure (XANES) region shows weak preedge transitions (1s \rightarrow 3d) at ~7112.5 eV and a pronounced rising edge (1s \rightarrow 4p) at \sim 7120.9 eV (Figure 2B). These features are at higher energy than those observed for planar FeN4 Fe(II) centers (i.e., 7112 eV and 7117 eV)^{12a,12b} suggesting the presence of Fe(III) centers. Notably the XANES spectra for Fe₄(THT)₂ and the LixFe₃(THT)₂ series all have identical edge positions (Figure 2B inset) and are similar to a semiconducting MOF with square planar iron(III)-bis(dithiolene) motifs.^{12c} These results are consistent with Fe(III) oxidation states across the series. Some of the more subtle differences in intensities for the edge features likely arise from electronic structure changes on the Fe center induced by ligand-based oxidation (Figure S27). Fitting EXAFS spectra in R-space and k-space based on the structural models all afford consistent results with reasonable Fe-S bond lengths (Figures S28, S29, Table S5).¹³

Further information on the oxidation and spin state of the Fe centers was obtained from ⁵⁷Fe Mössbauer spectroscopy. The experimental data and fits of $\mathbf{Fe_4(THT)_2}$ show three distinct sets of signals, with isomer shifts $(\delta, \text{mm/s})$ of 0.307(1), 0.340(8), and 0.437(6) and quadrupole splittings (ΔE_Q , mm/s) of 2.874(3), 2.288(9), and 0.965(11) (Figure S31). The first two signals have similar parameters to those found in intermediate spin S = 3/2 Fe(III) bis(dithiolene) complexes.¹³ The third signal is best assigned as high-spin Fe(III) and is reasonably attributed to

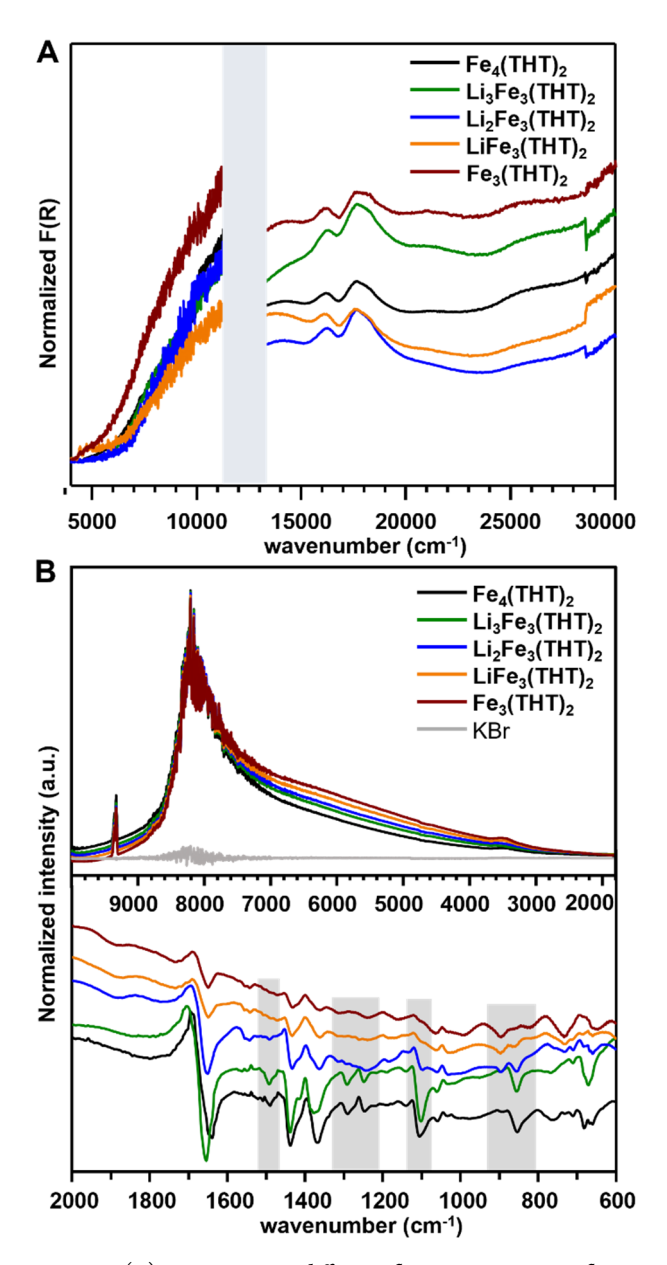


Figure 3. (A) UV-vis-NIR diffuse reflectance spectra. Inflection around 12000 cm⁻¹ and 2900 cm⁻¹ are due to lamp change and is covered by a gray box; F(R) is the Kubelka-Munk conversion of the raw diffuse reflectance. (B) FT-IR spectra recorded in transmission mode. Different vibrational features for the THT linkers in the redox series are highlighted in grey boxes (bottom).

additional charge balancing counter cations with a different coordination geometry. We propose that the two sets of Fe(III) bis(dithiolene) signals arise from electronic symmetry breaking induced by the additional Fe(III) counter cation. This hypothesis is supported by the fact that only one Fe species (δ : 0.349(1) mm/s, $\Delta E_{\rm Q}$: 2.909(1) mm/s) is observed in the lithium exchanged material Li₃Fe₃(THT)₂ (Figures 2C and S32). TheLi_xFe₃(THT)₂ materials all have similar Mössbauer parameters supporting constant Fe redox and spin states (Figures 2C and S31–S34). Finally, we note that there are two sets of Fe signals in the one-electron oxidized material Li₂Fe₃(THT)₂ but only one signal in LiFe₃(THT)₂ and Fe₃(THT)₂. We propose that this asymmetry arises from either cation induced structural disorder or electronic asymmetry from the

oxidized dithiolene motifs. The re-symmetrization of the signals upon further oxidation in LiFe₃(THT)₂ and Fe₃(THT)₂ may suggest greater electronic delocalization which may lead to higher conductivity (see below and the SI for a more detailed discussion on component oxidation states).

Bulk Electronic Structure

All of the Fe₃(THT)₃ materials display an intense broad absorption from 21000 to 4000 cm⁻¹ by UV-vis-NIR diffuse reflectance spectroscopy (Figure 3A). Fourier-transform infrared (FT-IR) spectroscopy also shows this absorption with a rise at ~3000 cm⁻¹ (Figure 3B top). A direct band gap Tauc analysis gives absorption edge values of 0.42-0.46 eV (Figure S35). These small band gaps are similar to those reported for $Fe_3(THT)_2(NH_4)_3^{9c}$ and **FeTHT**^{9d} and likely arises from the covalent Fe(III) bis(dithiolene) units and the extended conjugation in the 2D sheets. We note the emergence of weak signals at around 900 cm⁻¹ and a reduction of features at around 860 cm⁻¹, 1100 cm⁻¹, 1300 cm⁻¹, and 1500 cm⁻¹ upon oxidation (Figure 3B bottom). We also notice an emergence of weak signals at around 900 cm⁻¹ upon oxidation by Raman spectroscopy (Figure S26a). We therefore tentatively assign the 860 cm⁻¹ feature to v_{C-S} stretching modes and the 900 cm⁻¹ feature to more oxidized v_{C-S} features based on literature values. ¹⁵ All the other features observed are likely associated with vcc aromatic ring vibrations.

The bulk electrical conductivity (σ) of these five materials was measured with two-probe measurements on pressed pellets (Figures S36–S40). The average σ is $2.1(3)\times10^{-4}$ Scm⁻¹ for **Fe₄(THT)**₂ and $3.0(1)\times10^{-6}$ Scm⁻¹ for Li₃Fe₃(THT)₂. This reduced conductivity is unsurprising as the expanded interlayer distance (~0.15 Å) and additional cations likely weaken the interlayer interactions. However, the conductivity increases over 10,000-fold to 5.7(4)- $9.8(6)\times10^{-2}$ Scm⁻¹ in the oxidized Li_xFe₃(THT)₂(x=2-0) materials which is quite high although not as high as the best known conductive coordination polymers.4e We hypothesized that the increased conductivity may arise from the elimination of alkali cations, a contracted interlayer distance, or an increased number of radicals on the organic ligand compared to $Li_3Fe_3(THT)_2$. Variabletemperature conductivity measurements from 100-298 K exhibit increasing resistance upon cooling consistent with semiconducting behavior in these materials (Figures S41-S45). Satisfactory fits using a nearest-neighbor hopping (NNH) model¹⁶ can only be obtained in the high-temperature region, especially for $Li_3Fe_3(THT)_2$, resulting in small activation energies (E_a) that decrease slightly upon oxidation (Figure 4A, 0.197 eV to 0.062 eV). Better linear fits over the whole temperature range are obtained with a Mott variable-range hopping model¹⁷ with a decreasing trend in T_0 across the Li_xFe₃(THT)₂ redox series (Figure S46). This trend may indicate an approach to more band-like conduction possibly induced by sulfur vacancies upon oxidation.¹⁸ Taken together, these conductivity measurements indicate that these materials are low band gap semiconductors with multiple conduction mechanisms. The large change in conductivity illustrates how extensive redox tuning in these materials can change their physical properties.

The thermoelectric properties display an opposite trend to the above conductivity properties, namely **Li**₃**Fe**₃(**THT**)₂ has the highest Seebeck coefficient (*S*, +854.8 μV K⁻¹) with dropping values upon oxidation (Figure 4B and Table S6). Furthermore, a p-type to

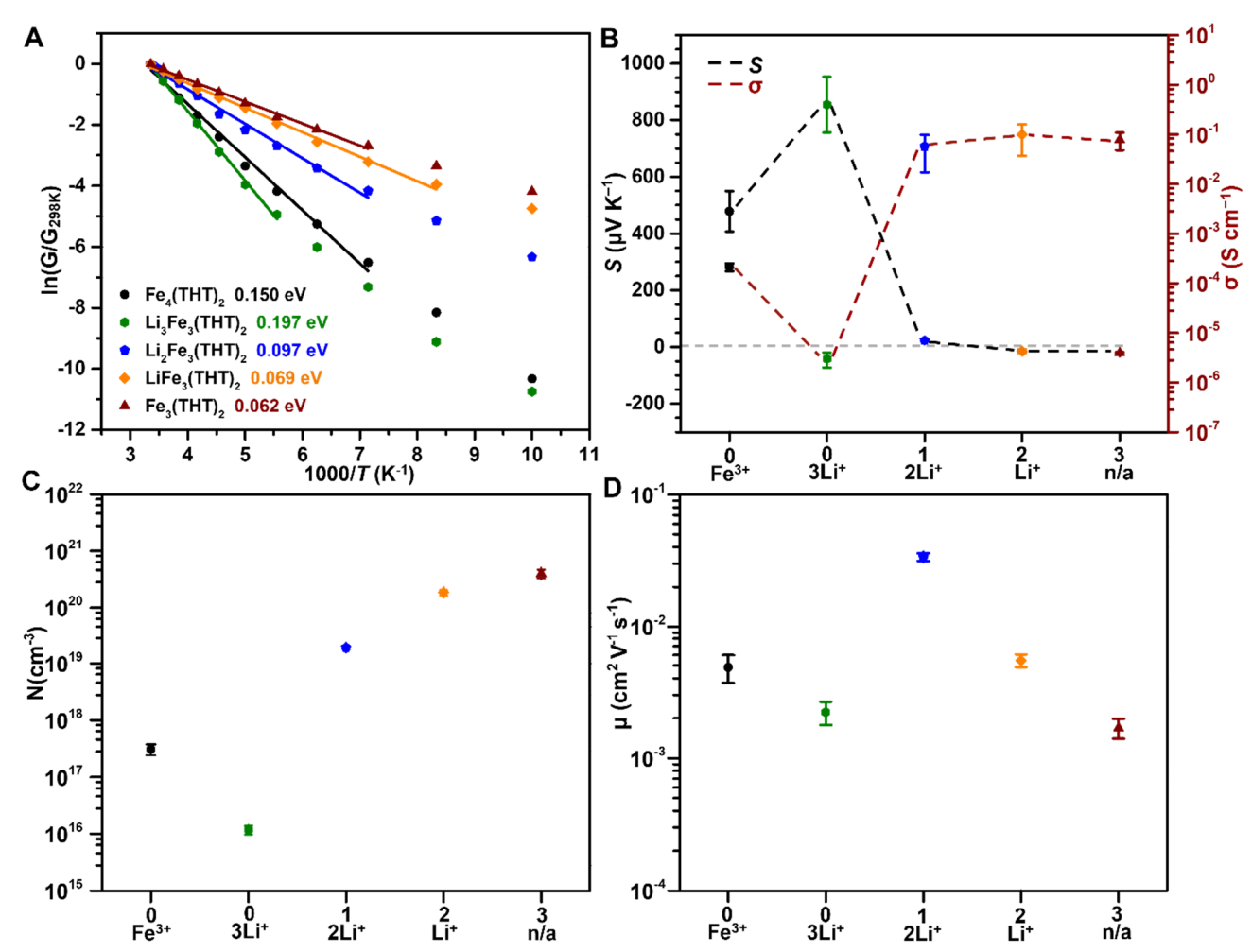


Figure 4. (A) Variable-temperature conductance (G) data (dots) and Arrhenius fitting (solid lines) in the high temperature range for **Fe**₄(**THT**)₂ and redox series **Li**_x**Fe**₃(**THT**)₂. Activation energy is indicated. (B) The Seebeck coefficient (S) and the conductivity (σ) plot against the counterion and oxidation level. (C) Summary of d.c. Hall charge carrier concentration (N) at room temperature as a function of counterion and oxidation level. (D) Calculated Hall charge mobility (μ) at room temperature as a function of counterion and oxidation level.

n-type transition is observed between Li₂Fe₃(THT)₂ and $LiFe_3(THT)_2$. The dominant p-type character in $Fe_4(THT)_2$, Li₃Fe₃(THT)₂ and Li₂Fe₃(THT)₂ may originate from the Fe(III) centers acting as acceptors as proposed in other Fe-based MOFs. 9c,19 The transition to n-type behavior on oxidation may therefore be ascribed to the generation of unpaired ligand-based electrons as donors and ultimately change the dominant carrier type in the system. We note that most 2D semiconductors are n-type due to electron doping from interfacial charge impurities and defects; the search for p-type 2D semiconductors as well as p-n switchable materials is of great interest.²⁰ Here, we demonstrate synthetic tuning to realize p-type 2D semiconductors as well as p-n switching via redox manipulations. The thermoelectric power factor $(S^2\sigma)$ is very similar (2-5 nW m⁻¹ K⁻²) for Fe₄(THT)₂ and Li_xFe₃(THT)₂ (x= 2-0), but slightly lower (0.2 nW m⁻¹ K⁻²) for $Li_3Fe_3(THT)_2$ (Figure S47). This relatively constant power factor across different redox-states is common in semiconductor thermoelectric materials due to the inverse relationship between S and σ from the Mott relation.²¹ It remains to be seen whether alternative designs in these unconventional MOF thermoelectrics can optimize S, o, or the thermal conductivity (κ_e) to overcome this limitation.²²

The similar hopping energies in these materials led us to hypothesize that the trends in conductivity and thermoelectric properties arise from changes in carrier densities upon oxidation. To test this hypothesis, Hall effect measurements were conducted on pressed pellets (see experimental section for details). In general, the measured Hall carrier concentration (N) at room temperature follows the same trend as the bulk electrical conductivity. Specifically, the Hall carrier concentration in Fe₄(THT)₂ (3.10(6)×10¹⁷ cm⁻³) decreases after cation exchange in $\text{Li}_3\text{Fe}_3(\text{THT})_2$ (1.19(2)×10¹⁶ cm⁻³). Upon oxidation, the value increases 10,000-fold from $\text{Li}_3\text{Fe}_3(\text{THT})_2$ (1.19(2)×10¹⁶ cm⁻³) to $Fe_3(THT)_2$ (3.97(7)×10²⁰ cm⁻³) and continues increasing, albeit at a slower rate, in the more highly oxidized materials (Figures 4C and S48-S50). The trend is also consistent with the Seebeck coefficient as the carrier concentration increases, the Seebeck coefficient decreases. In contrast, the Hall mobility (μ) remains comparatively constant except for a slightly higher value in Li₂Fe₃(THT)₂ (Figure 4D). All these results support the hypothesis that the carrier density primarily determines the electrical conductivity according to the relation $\sigma = Ne\mu$ (where *e* is the electron charge). We propose that replacement of charge balancing Fe(III) cations (as electron acceptors) with Li+ could decrease the carrier density moderately;

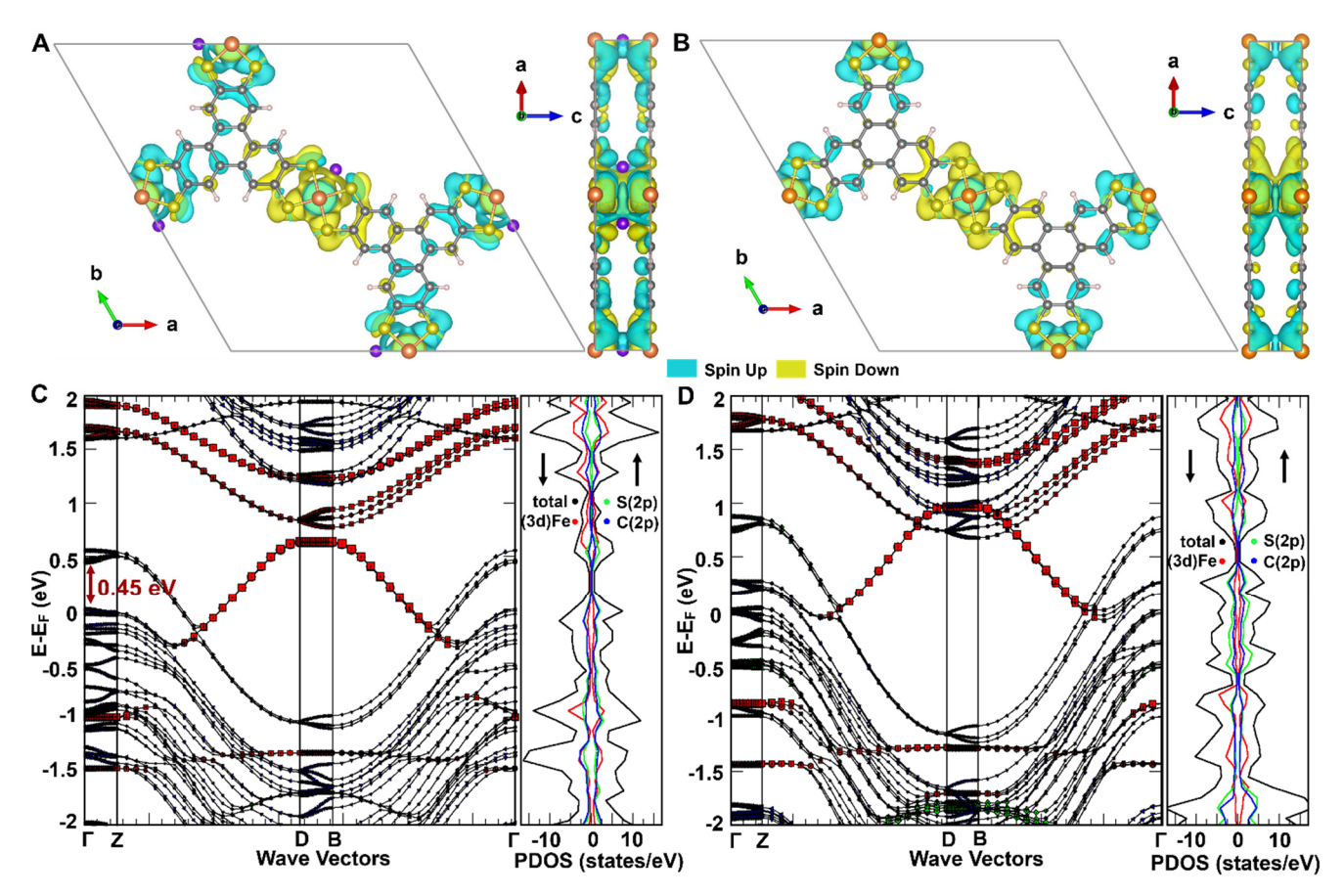


Figure 5. Spin density iso-surface (isovalue 0.0005 e/A³) of the anti-ferromagnetic state of (A) Li₃Fe₃(THT)₂ and (B) Fe₃(THT)₂ along the c-axis and b-axis of the unit cell. Color code: orange, Fe; yellow, S; grey, C; purple, Li; pink, H. Projected band structure and projected DOS of (C) Li₃Fe₃(THT)₂ and (D) Fe₃(THT)₂ computed from Hubbard corrected PBEsol-D3 (BJ) functional.

while adding unpaired ligand-based electrons (as formal electron donors) increases the carrier density dramatically. Variable-temperature Hall effect measurements were also performed to probe the correlation between the temperature and the carrier concentration (Figures S51–S55, Tables S7–S11). These measurements show a clear decrease in carrier concentration with decreasing temperature, and the calculated activation energies are almost identical to the values from the variable-temperature conductivity measurements. These observations further support that thermally excited carriers are responsible for the electrical conductivity in all five materials.

Band Structure Calculation by DFT

Periodic density functional theory (DFT) calculations were performed to examine the geometric and electronic structure of the Li_xFe₃(THT)₂ redox series. The PBEsol-D3 (BJ)²³ exchange correlation functional, which has been extensively employed to predict MOF structures and properties, ²⁴ was used with a dispersion correction²⁵ as implemented in VASP²⁶ (see supporting information). All calculations were converged to an antiferromagnetically coupled electronic ground state both during geometry optimization and single point calculations, consistent with the experimental dc magnetic susceptibility data (see below). Alternate Fe-centers were assigned opposite or anti-parallel spins and the radicals on the sulfur centers were allowed to relax freely. The computed bond lengths are reported in Table S12 and are in good agreement with experimental values.

We computed the projected density-of-states (pDOS) and the band structure using a high-symmetry K-point grid and a higher energy cut-off (800 eV). During the band and pDOS calculations we used a strong on-site Coulomb (U = 4 eV) and exchange (I = 1 eV) Hubbard correction²⁷ of localized d-orbitals on the Fe-center by performing single-point calculations at the optimized geometry. The experimental magnetic, Mössbauer, and other experimental data corroborate redox non-innocent character of the THT ligand and unpaired electrons on the Fe-centers. The spin density iso-surfaces (Figure 5A, 5B) of Li₃Fe₃(THT)₂ and Fe₃(THT)₂ support this picture; the presence of alpha and beta spin populations on Fe and as well as on the S and C atoms of the THT ligand suggest significant spin delocalization and polarization of the Fe-center and the THT ligand. This supports the fact that unpaired electrons are delocalized on the THT ligand and the Fe-centers and also that the Fe-centers in the unit cell are anti-ferromagnetically aligned to stabilize the lowest possible spin configuration.

The selected U and J values (U = 4 eV and J = 1 eV) accurately reproduce the band gaps of the Fe-based MOFs and are also consistent with previously reported U and J values for similar systems. ^{6d,9d} The loosely bound unpaired electrons (equivalently radicals) in the ligand framework result in several bands with small bandwidths in all of the band structures. This convolutes precise band gap estimations in the oxidized materials. However, $\mathbf{Li_3Fe_3(THT)_2}$ is predicted to have a distinct band gap of 0.45 eV near the Fermi level (Figure 5C). The mid band gap states for

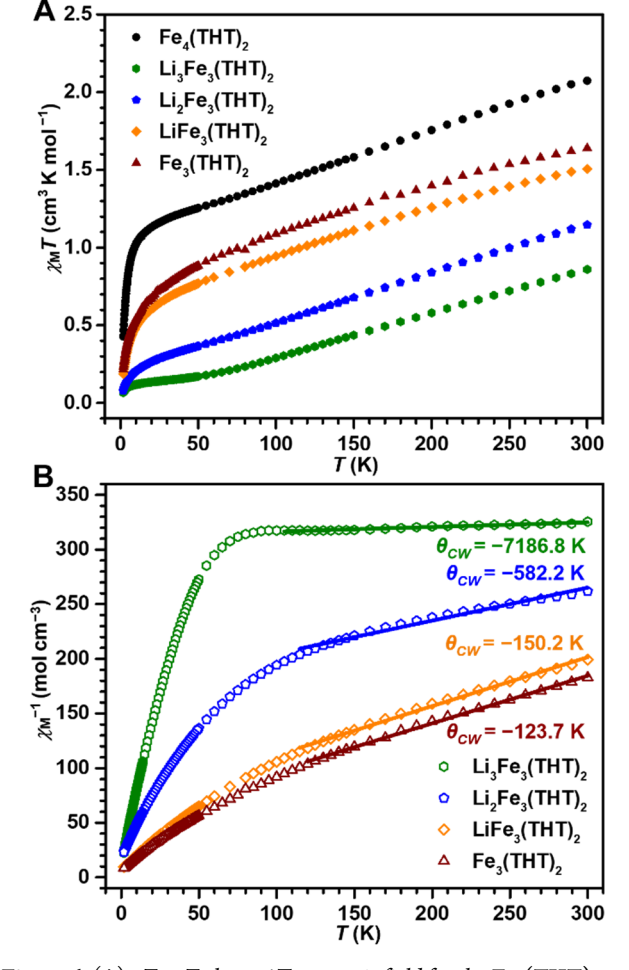


Figure 6. (A) χT vs T plot at 1T magnetic field for the $\mathbf{Fe_4(THT)_2}$ and $\mathbf{Li_xFe_3(THT)_2}$ (x= 3-0) materials. (B) χ_{M}^{-1} vs T plot (dots) and Curie-Weiss fit (solid lines) for $\mathbf{Li_xFe_3(THT)_2}$ (x=3-0) materials at high temperature range. The decreasing Weiss constants (θ_{CW}) implies weakening antiferromagnetic interactions across the redox series.

Fe₃(THT)₂ occur between 0.0-0.16 eV and between 0.27-0.75 eV; for LiFe₃(THT)₂ they occur between 0.18-0.46 eV and from -0.125-0.05 eV, and for Li₂Fe₃(THT)₂ they occur between -0.28-0.11 eV and from 0.12-0.46 eV (Figures 5C,5D and S57). This trend in the computed band gap is consistent with the experimentally observed trends of the optical band gaps (0.42-0.46 eV) and activation energies (0.062-0.197 eV) in the four materials. We also notice that the valence band is dominated by sulfur and carbon 2p electrons, while the conduction band consists of sulfur and carbon 2p as well as Fe-3d orbitals.

Magnetic properties

The experimental $\chi_M T$ values (per formula unit) of these materials all show a general decreasing trend with temperature suggesting antiferromagnetic interactions (Figure 6A). The $\chi_M T$ value of $\text{Li}_3\text{Fe}_3(\text{THT})_2$ at 300 K is 0.86 cm³ K mol⁻¹ which is smaller than the theoretical spin-only value for three magnetically uncoupled S=1/2 Fe centers ($\chi_M T \approx 1.13 \text{ cm}^3 \text{ K mol}^{-1}$) or S=3/2 Fe centers ($\chi_M T \approx 5.63 \text{ cm}^3 \text{ K mol}^{-1}$). In comparison, $\text{Fe}_4(\text{THT})_2$ has a larger $\chi_M T$ value of 2.07 cm³ K mol⁻¹ at 300 K which may be attributed to the additional paramagnetic Fe(III) center. Interestingly, the $\chi_M T$ value of the redox series increases upon oxidation. The increases in $\chi_M T$

between $\text{Li}_3\text{Fe}_3(\text{THT})_2$ (0.86 cm³ K mol⁻¹), $\text{Li}_2\text{Fe}_3(\text{THT})_2$ (1.15 cm³ K mol⁻¹), and $\text{LiFe}_3(\text{THT})_2$ (1.51 cm³ K mol⁻¹) roughly correspond to the addition of a weakly coupled S = 1/2 linker ($\chi_M T \approx 0.375$ cm³ K mol⁻¹). This observation suggests that any radical linkers couple weakly with the Fe centers. However, $\text{Fe}_3(\text{THT})_2$ ($\chi_M T \approx 1.64$ cm³ K mol⁻¹) does not follow this same increment which may be rationalized by electronic delocalization of the organic radicals.

The magnetic data was further analyzed by fitting the χ_{M}^{-1} data to the Curie-Weiss law and a suitable linear fit can only be obtained in the high temperature region (300 K to 120 K). All fits reveal negative Weiss constants (θ_{CW}) with decreasing values of -7186.8 K, -582.2 K, -150.2 K and -123.7 K for the $\text{Li}_x\text{Fe}_3(\text{THT})_2 (x=3-0)$ materials, consistent with dominant antiferromagnetic character (Figure 6B). We hypothesize that the strong antiferromagnetic interaction at high temperature arises from metal-metal coupling along the 1D FeS4 stacks. And the decreasing trend could be due to the addition of unpaired electrons in the linkers upon oxidation that may weaken these antiferromagnetic interactions. A similar trend has been observed in a molecular system where J_{FeFe} decreases from −250 cm⁻¹ to −200 cm⁻¹ with the addition of metal–radical ligand couplings of -200 and -140 cm⁻¹. Notably, the $\chi_{\rm M}^{-1}$ (or $\chi_{\rm M} T$) values decline more rapidly below 50 K, suggesting the presence of other interactions. We tentatively propose a complicated coupling scheme with competing intra-/inter-2D sheet and intra-/inter-1D FeS₄ chain interactions. Finally, we note that the low temperature region of this data shows no inflection features and variabletemperature zero-field-cooled and field-cooled DC magnetization data shows no divergence for all the materials (Figures S58-S62). This supports the absence of any long-range ordering which is perhaps unsurprising given the geometrically frustrated Kagomé lattice of the metal centers as discussed more thoroughly in a previously reported 2D semiconductive MOF.²⁸ At the least this data adds to the growing body of research suggesting that strongly correlated 2D MOFs with unique topologies are interesting platforms to explore unconventional magnetic phenomena.

Conclusions

Redox-active MOFs provide a uniquely tunable scaffold for materials properties, with several examples showing conductivity or magnetic tuning over 1-2 redox events. Here we report a robust protocol for the bulk synthesis of crystalline 2D semiconducting MOFs featuring Fe bis(dithiolene) motifs that can be tuned over a remarkable four distinct redox-states. Through a battery of spectroscopic methods, we confirmed ligand-centered oxidation during redox modulation. The physical properties, including conductivity, thermoelectric behavior, concentrations, and magnetic interactions all respond dramatically to redox tuning. Oxidation leads to 10,000-fold greater conductivity, p- to n-type carrier switching, and modulation of antiferromagnetic coupling. Hall effect experiments further suggest that these changes in charge transport for the bulk materials are predominantly gated by carrier densities with little change in mobilities. These results elucidate important electronic design principles in 2D conducting MOFs and also illustrate the broad tunability of these materials over many redox-states.

Experimental Section

General consideration: All material syntheses and characterizations were performed under an inert atmosphere of dry N_2 using a Schlenk line, in a MBraun UNIIab glovebox, or under N_2 protection unless otherwise noted. Dimethylformamide (DMF) and acetonitrile (MeCN) used in preparing the materials were initially dried on a solvent purification system from Pure Process Technology and were further treated by passing through activated alumina and stored over 4 Å molecular sieves in the glovebox. Petroleum ether and dicloromethane (DCM) were dried on the same solvent purification system and stored over 4 Å molecular sieves. All other chemicals were purchased from commercial sources and used as received unless noted. NMR measurements were performed on Bruker DRX 400 spectrometers.

Synthesis of ligand SnTHT. The precursor compounds 2,3,6,7,10,11-hexabromotriphenylene, 2,3,6,7,10,11-Hexabenzylmercaptyltriphenylene, sodium triphenylenehexathiolate were obtained by following previous literature procedures.9a The stannylated precursor SnTHT was obtained with adapted procedures from a similar literature report. 10 A dry reaction mixture of the sodium triphenylenehexathiolate (4 mmol, 2.2 g) was taken into the glovebox and washed with diethyl ether two times. The resulting white residue was then added into a solution of di-n-butyltin(IV) dichloride (24 mmol, 7.3 g) in MeCN. The reaction was stirred at room temperature overnight and the solvent was then removed by vacuum. After that, 50 mL DCM was added, and the mixture was filtered through silica/celite layers in a 60 mL fritted funnel to get rid of the insoluble byproducts. The filtrate was dried under vacuum and the resulting residue was washed with pet ether three times $(3 \times 30 \text{ mL})$ through a fritted funnel to yield the target compound as white powder (2.0 g, yield 45%). ¹H NMR (CDCl₃, 300 K): 0.92 (t, *J* = 6.3 Hz, 3H), 1.41 (m, 2H), 1.70-1.78 (m, 4H), 8.52 (s, 1H). ¹³C NMR (CDCl₃, 300 K): 13.72, 21.82, 26.80, 28.07, 123.76, 126.08, 138.46.

Synthesis of Fe₄(THT)₂. The ligand precursor SnTHT (0.15 mmol, 167 mg) was dissolved in 6 mL of DMF in a vial in a N₂ filled glovebox. Anhydrous FeCl₂ (1.35 mmol, 171 mg) dissolved in 6 mL of DMF was added to the pre-ligand solution slowly, followed by the addition of thiophenol (3.0 mmol, 300 μ L). The reaction mixture was heated at 120 °C for 3 days in the glovebox. The mother liquor was decanted after cooling to room temperature. The remaining solid was washed thoroughly with fresh DMF (3×15 mL) and CH₃CN (3×15 mL) by soaking the solid in fresh solvent for few hours followed by decanting. The resulting black powder was dried under vacuum overnight at room temperature (47 mg, yield 60%). For safety, scaled-up preparations did not use a larger individual vessel but instead six parallel vials were set up each time. Characterization across different batches supports batch-to-batch consistency.

Synthesis of Li₃Fe₃(THT)₂ by cation exchange. Freshly made Fe₄(THT)₂ (~100 mg) was soaked in 0.5 M LiPF₆ solutions (3×15 mL, DMF) at 50 °C for three days, decanting the mother liquor and adding fresh solution each day. After these three soaks, the remaining solid was washed thoroughly with fresh DMF (3×15 mL) and CH₃CN (3×15 mL) by soaking the solid in the fresh solvent for few hours followed by decanting. The resulting black powder was

dried under vacuum overnight at room temperature (90 mg, yield 90%).

Synthesis of material Li_xFe₃(THT)₂ (x= 2–0) by stoichiometric redox modulation. Freshly made Li₃Fe₃(THT)₂ (96 mg, 0.078 mmol) was soaked in DMF with the appropriate stoichiometric amount of ferrocenium hexafluorophosphate (i.e., 1eq, 0.078 mmol, 25.8 mg; 2eq, 0.156 mmol, 51.6 mg; 3eq, 0.234 mmol, 77.4 mg) at room temperature for two days. The mother liquor was decanted. The remaining solid was washed thoroughly with fresh DMF (3×15 mL) and CH₃CN (3×15 mL) by soaking the solid in the fresh solvent for few hours each time. The resulting black powder was dried under vacuum overnight at room temperature (~80 mg, yield 86%). We note that the resulting powder becomes visibly more brown than black when using an excess amount of ferrocenium hexafluorophosphate (i.e., 10 eq and 20 eq).

X-Ray Powder Diffraction. Laboratory PXRD data were acquired on a Rigaku MiniFlex benchtop X-ray diffractometer equipped with CuK α radiation in Bragg-Brentano reflection geometry. Synchrotron X-ray powder diffraction data collections were carried out at 295 K at beamline 11-BM of the Advanced Photon Source at Argonne National Laboratory using a calibrated wavelength of $\lambda = 0.458095$ Å for $\text{Li}_3\text{Fe}_3(\text{THT})_2$ and $\lambda = 0.458963$ Å for the other four materials. The powder was sealed in thin-wall capillary tubes to avoid air exposure. The data analysis was carried out using GSAS-II software.

Gas Chromatography (GC). The existence of of H_2 and CO in the atmosphere of material synthesis reactions were confirmed on an Agilent 7890B GC with FID and TCD Detectors. Column: Carboxen-1010 PLOT (30 m \times 0.53 mm); oven: 250 °C; injection: 200 °C; flow rate: N_2 , 3.0 mL/min; injection: 10.0 μ L valve injection. The retention time of H_2 (~0.61 min by TCD) and CO (~0.99 min by FID) were determined by control experiments.

Scanning Electron Microscopy (SEM). SEM images were taken on a Carl Zeiss Merlin electron microscope using the In-Lens detector in the Materials Research Science and Engineering Center (MRSEC) at the University of Chicago. The sample powder was dispersed on the conductive tape substrates and an accelerating voltage of 5.00 kV was applied for the measurement.

Transmission Electron Microscopy (TEM). TEM images were taken on the FEI Tecnai F30 electron microscope. The sample powder was dispersed in MeCN and sonicated for about five minutes before loading onto the copper grid. High-resolution transmission electron microscopy (HRTEM) images were processed in the ImageJ software.

Nitrogen Adsorption Measurements. Crystalline solid was transferred to a pre-weighed analysis tube in the glovebox and capped with a Transeal. The sample tube was then transferred to a Micrometrics ASAP 2020 Plus gas adsorption analyzer and degassed at a rate of $1.0\,^{\circ}$ C/min from room temperature to a final temperature of 70 °C. The sample was further activated at 70 °C for three days until an outgas rate of less than 1 mTorr/min was observed. The N_2 adsorption isotherm at 77 K was measured in liquid nitrogen. After the experiment, the PXRD pattern of the sample was checked, and the crystallinity was maintained.

Inductively Coupled Plasma Optical Emission Spectroscopy (ICP-OES). The ICP-OES analysis was carried out

using an Agilent 700 series spectrometer. Digestion procedures were adapted from a reported literature. Digestion procedures were adapted from a reported literature. Around 2 mg of each material was digested in 1.0 mL HNO3 and 1.0 mL $\rm H_2O_2$ (both are trace metal grade) in tightly sealed high-density polyethylene (HDPE) centrifuge tubes overnight. The solution was further diluted to the 1–25 ppm range with ultrafiltered deionized water. The absolute element concentration (Table S1) was obtained from a freshly made external calibration curve. The averaged element concentration from two characteristic emission wavelengths for each element was used to calculate the final Li/Fe/S ratio.

X-ray fluorescence spectroscopy (XRF). XRF spectra were collected on a Rigaku NEX DE VS spectrometer under a He atmosphere. The sample was prepared as a pressed pellet (7mm diam) and the results were externally calibrated to a commercial multielement standard.

X-ray Photoelectron Spectroscopy (XPS). XPS spectra were collected on an AXIS Nova spectrometer (Kratos Analytical) equipped with a monochromatic Al K α X-ray source. The instrument work function was calibrated to give an Au $4f_{7/2}$ metallic gold binding energy of 83.95 eV. For calibration purposes, the binding energies were referenced to C 1s peak at 284.8 eV. Survey spectra were collected with a step size of 1 and 160 eV pass energy. The high-resolution spectra were collected with a pass energy of 40 and 0.1 eV step size.

X-ray Absorption Spectroscopy (XAS). Powder samples were diluted with polypropylene and pressed into pellets for data collection. The sample pellets were further sealed in a Teflon washer with Kapton tape to avoid air exposure. Fe K-edge data were acquired at the MRCAT 10-BM beam line in transmission mode at room temperature. A metallic iron foil standard was used as a reference for energy calibration and was measured simultaneously with experimental samples.

Mössbauer Spectroscopy. Zero-field iron-57 Mössbauer spectra were obtained at 77 K with a constant acceleration spectrometer and a cobalt-57 rhodium source. Prior to measurements, the spectrometer was calibrated at 295 K with α-iron foil. The sample was encased in Paratone-N oil and placed in a polyethylene sample cup inside a N_2 filled glovebox. The spectra were analyzed using the WMOSS Mössbauer Spectral Analysis Software (www.wmoss.org).

UV–Vis–NIR Spectroscopy. Solid UV–vis–NIR diffuse reflectance spectra were collected on a CARY 5000 spectrophotometer. Powder samples were loaded in a Praying Mantis air-free diffuse reflectance cell with KBr powder as the non-adsorbing matrix. The Kubelka-Munk conversion of the raw diffuse reflectance spectrum was obtained by applying the formula $F(R) = (1-R)^2/2R$.

Raman Spectroscopy. Powder samples for Raman were pressed into pellets and sealed between two glass slide using an imaging spacer in the glovebox. Raman spectra were obtained with a Horiba LabRamHR Evolution confocal microscope. A Si (111) wafer was used for calibration. The sample was excited using a 633 nm light source operating at 2~10 % of its maximum power and using 100x long path objective and a 600 mm⁻¹ grating.

Fourier-transform infrared spectroscopy (FT-IR). Powder samples for FT-IR were pressed into pellets in a potassium bromide matrix. Spectra were acquired in transmission mode on a Bruker

Tensor II spectrometer with MCT detector operated at 77 K. Data was processed with background subtractions.

Conductivity Measurements. Room temperature electrical conductivity measurements were performed in a two-contact geometry using a BASi Epsilon potentiostation/Galvano station fitted to an N2 glovebox. Samples were prepared as pressed pellets clamped between two brass electrodes (4.8 mm diam, 0.178 cm² area.) in a glass sleeve using a hand press. Sample pellet thicknesses were measured with a caliper and were typically in the range of 200 to 500 µm. Linear sweep voltammetry was conducted with the reference and counter electrode terminals connected to one electrode and the working electrode terminal to the other. The resulting data were fit to a straight line to obtain the sample resistance. The area of the pellet is 0.178 cm². The conductivity is calculated using the formula of $\sigma = \frac{I}{V} \times \frac{l}{A}$ where $\frac{I}{V}$ is the slope of the fitting line, l is the thickness of the pellet and A is the area. Variabletemperature electrical conductivity measurements were performed under vacuum with a custom designed Montana instruments S50 cryostation coupled to a PCI-6221 multifunction I/O device (National Instruments) and a current preamplifier (Stanford research systems, SR570). Rectangular sample pellets (6mm × 3mm) were prepared in the glovebox using a TMAX laboratory manual hydraulic press under a pressure of 3 tons, and fitted to a Kyocera ceramic dual inline package through indium-wire connections (Figure S41a). The package was sealed with Kapton tape on the top to avoid air exposure during sample loading. Ohmic I–V profiles were observed for all temperatures from 100 K to 298 K with a 20 K interval, and a linear fit of the I-V curve was used to get the conductance (G) of the sample.

Seebeck Coefficient Measurement. The Seebeck coefficient measurements were performed using a custom-designed probe station in an argon glovebox with a well-established method.31 Around 20 mg sample powder was pressed into a pellet with a diameter of 8 mm using a TMAX Laboratory Manual Hydraulic Press under a pressure of 3 tons. Gold electrical contacts (~75 nm thick) were deposited onto the pressed pellet (~200 µm thick) of bulk sample powder via thermal evaporation) in a glovebox with an internally mounted Angstrom Covap PVD at a rate of 0.2 nm/s. Two thermocouples were used to collect the hot and cold side temperatures, and another two probes were used to measure the corresponding voltage value. A delay of 200 s was adopted for voltage measurements to allow a steady-state temperature gradient and voltage. The Seebeck coefficient was calculated from the slope of a linear fit for the ΔV vs ΔT plot. For each sample, both a forward and a reverse scan were carried out to obtain an average Seebeck value and a coefficient of 1.2 was divided to adjust the geometry.³²

Hall Effect Measurement. The Hall effect measurements were carried out on a Quantum Design Physical Property Measurement System (PPMS) using the Model 6000 controller. Specific gold electrical contacts (~75 nm thick) were deposited onto the pressed sample pellets (6mm \times 3mm) to form a Hall bar (Figure S48a) in an Argon filled glovebox. The sample pellet was further mounted to a DC Resistivity/ETO Sample Puck (P102) through indium-wire bonding (Figure S48b) in a N₂ filled glovebox. The sample pellet was exposed to air for ~1 minute when loading the puck to the air-free chamber. An immediate resistance check showed a noticeable resistance decrease (10%~20%) for the Fe4(THT)₂ and

Li₃Fe₃(THT)₂, which indicated the carrier concentration of these two materials may be slightly overestimated by the experimental data. It is also worthwhile to mention that there is a slow monotonic drift of background voltage with time,³³ which is independent of magnetic field and common in Hall measurements of resistive samples. In our case this drift is negligible due to the short time scanning the magnetic field (\sim 7 mins) for each individual measurement and the comparatively large slope from the relative low carrier concentration of each sample.

In order to check the reproducibility and reliability of the Hall effect, three individual measurements were conducted for each sample pellet at each temperature point by varying the applied current and magnetic field direction (i.e., I_1 , +B; I_2 , +B; I_2 , -B). A non-zero offset voltage at zero field was observed, which is probably due to a geometry misalignment ($V_{\rm Mis}$, no field dependence), thermal electric effect ($V_{\rm TE}$, no current dependence) and others. However, the absolute value of the slop ($dR_{\rm Mea}/dB$) from linear fitting of the measured resistance ($R_{\rm Mea}$) vs magnetic field (B) were consistent across all three measurements. These findings confirm the reproducibility and reliability of the Hall effect using our method. Thus, the values of the slops were further used to calculate the Hall coefficient ($R_{\rm H}$), Hall carrier concentration (N) and mobility (μ) by the equation below:

$$\begin{split} V_{\text{Mea}} = & V_{\text{Hall}} + V_{\text{Mis}} + V_{\text{TE}} \\ V_{\text{Mea}} = & IR_{\text{H}}B/t + \alpha IR_0 + V_{\text{TE}} \\ R_{\text{Mea}} = & R_{\text{H}}B/t + \alpha R_0 + V_{\text{TE}}/I \\ R_{\text{H}} = & dR_{\text{Mea}}/dB \bullet t \\ N = & \frac{1}{R_{\text{H}} \, e} \\ \mu = & \frac{\sigma}{N_{\text{P}}} \end{split}$$

where t is the thickness of the pellet, σ is the electrical conductivity, and e is the electron charge (1.6×10⁻¹⁹ C).

Magnetic Measurements. Magnetic measurements were performed on a Quantum Design MPMS3 SQUID magnetometer. The bulk powder of each sample $(20{\sim}30~\text{mg})$ was measured accurately and then suspended in an eicosane matrix in a polycarbonate capsule to prevent movement and protect the sample from incidental air exposure in a N_2 filled glovebox. Diamagnetic corrections for the capsule and eicosane were made by measuring temperature vs moment in triplicate for each sample to determine a moment per gram correction. Diamagnetic corrections for the sample itself were applied using Pascal's constants of each atom based on the formula of $Fe_4(THT)_2$ and $Li_xFe_3(THT)_2$.

Computational Methods. Periodic DFT calculations have been performed using Vienna Ab Initio Simulation Package (VASP v6.2.1).²⁶ The project augmented wave (PAW) method³⁴ was used with the revised Perdew-Burke-Ernzerhof for solids (PBEsol)²³ functional with the Grimme's van der Waals D3 correction with Becke-Johnson (BJ) damping.³⁵ The number of plane waves was selected for converging the energy cut-off at 500 eV during geometry optimization. The geometry was relaxed using a 2x2x15 Monkhorst-Pack K-points³⁶ grid which was also tested for convergence. We have focused the electronic structure calculations on the redox series since the physical properties response dramatically in the redox series. The unit cell was kept fixed to the Rietveld refined structures during the geometry optimization. It is notable that the positions of lithium in the unit cell can be effectively "disordered" (Figure S12a).

Thus, we have used the one of the symmetric structure models for the calculations and the corresponding lithium is shown to have an energetically favorable interaction with nearby S atoms (Figure S56). All the calculations were performed in a spin-polarized manner with an anti-ferromagnetic electronic configuration. The anti-ferromagnetic configuration was chosen by assigning the spin of the alternate Fe-centers to anti-parallel alignment of alpha and beta electrons. The anti-ferromagnetic configuration also found to be the ground state configuration according to the dc magnetic susceptibility data. To estimate the projected density of state (pDOS), and spin density iso-surface, single point calculations were carried out using a higher energy cut-off at 800 eV and high-symmetry K-point grids. For this, Coulomb and exchange interactions of the localized d-orbitals in Fe-centers were treated within the framework using DFT+U method. The effective Coulomb (U) and exchange (J) parameters were set at U = 4 eV and J = 1 eV which was also tested previously in similar systems. 6d,9d

ASSOCIATED CONTENT

Supporting Information

Additional experimental details and characterization data are included in supporting information. The Supporting Information is available free of charge on the ACS Publications website.

AUTHOR INFORMATION

Corresponding Author

jsanderson@uchicago.edu

ORCID

Lei Wang: 0000-0002-3778-2814 Arup Sarkar: 0000-0002-6880-8220 Garrett L. Grocke: 0000-0001-8661-5038 Shrayesh N. Patel: 0000-0003-3657-827X Alexander S. Filatov: 0000-0002-8378-1994 Laura Gagliardi: 0000-0001-5227-1396 John S. Anderson: 0000-0002-0730-3018

Notes

The authors declare no competing financial interests.

ACKNOWLEDGMENT

This research was supported by the U.S. National Science Foundation (DMR-2002367) and as part of the as part of the Catalyst Design for Decarbonization Center, an Energy Frontier Research Center funded by the U.S. Department of Energy, Office of Science, Basic Energy Sciences under Award No. DE-SC0023383 particularly for the computational work. Use of the Advanced Photon Source at 11-BM at Argonne National Laboratory was supported by the U.S. Department of Energy, Office of Science, Office of Basic Energy Sciences, under Contract DE-AC02-06CH11357. This work made use of the shared facilities at the University of Chicago Materials Research Science and Engineering Center (MRSEC), supported by National Science Foundation under award number DMR-2011854. We would like to acknowledge UChicago Research Computing Center (RCC) for the supercomputing facility. We thank Dr. Daniel L. M. Suess and Alexandra C. Brown (Massachusetts Institute of Technology) for the assistance with Mössbauer spectroscopy. We also thank Jiaze Xie for discussions on Hall effect measurements.

REFERENCES

- 1. (a) Xu, M.; Liang, T.; Shi, M.; Chen, H., Graphene-Like Two-Dimensional Materials. *Chem. Rev.* **2013**, *113* (5), 3766-3798. (b) Bhimanapati, G. R.; Lin, Z.; Meunier, V.; Jung, Y.; Cha, J.; Das, S.; Xiao, D.; Son, Y.; Strano, M. S.; Cooper, V. R.; Liang, L.; Louie, S. G.; Ringe, E.; Zhou, W.; Kim, S. S.; Naik, R. R.; Sumpter, B. G.; Terrones, H.; Xia, F.; Wang, Y.; Zhu, J.; Akinwande, D.; Alem, N.; Schuller, J. A.; Schaak, R. E.; Terrones, M.; Robinson, J. A., Recent Advances in Two-Dimensional Materials beyond Graphene. *ACS Nano* **2015**, *9* (12), 11509-11539.
- 2. (a) Manzeli, S.; Ovchinnikov, D.; Pasquier, D.; Yazyev, O. V.; Kis, A., 2D Transition Metal Dichalcogenides. *Nat. Rev. Mater.* **2017**, 2 (8), 17033. (b) Lin, H.; Zhang, Z.; Zhang, H.; Lin, K.-T.; Wen, X.; Liang, Y.; Fu, Y.; Lau, A. K. T.; Ma, T.; Qiu, C.-W.; Jia, B., Engineering van der Waals Materials for Advanced Metaphotonics. *Chem. Rev.* **2022**, 122 (19), 15204-15355. (c) Li, Y.; Yang, B.; Xu, S.; Huang, B.; Duan, W., Emergent Phenomena in Magnetic Two-Dimensional Materials and van der Waals Heterostructures. *ACS Appl. Electron. Mater.* **2022**, 4 (7), 3278-3302. (d) Liu, X.; Hersam, M. C., 2D Materials for Quantum Information science. *Nat. Rev. Mater.* **2019**, 4 (10), 669-684. (e) Lu, J. M.; Zheliuk, O.; Leermakers, I.; Yuan, N. F. Q.; Zeitler, U.; Law, K. T.; Ye, J. T., Evidence for Two-Dimensional Ising Superconductivity in Gated MoS₂. *Science* **2015**, 350 (6266), 1353-1357.
- 3. (a) Hmadeh, M.; Lu, Z.; Liu, Z.; Gándara, F.; Furukawa, H.; Wan, S.; Augustyn, V.; Chang, R.; Liao, L.; Zhou, F.; Perre, E.; Ozolins, V.; Suenaga, K.; Duan, X.; Dunn, B.; Yamamto, Y.; Terasaki, O.; Yaghi, O. M., New Porous Crystals of Extended Metal-Catecholates. *Chem. Mater.* 2012, 24 (18), 3511-3513. (b) Hendon, C. H.; Tiana, D.; Walsh, A. Conductive Metal-Organic Frameworks and Networks: Fact or Fantasy? *Phys. Chem. Chem. Phys.* 2012, 14, 13120-13132. (c) Rubio-Giménez, V.; Tatay, S.; Martí-Gastaldo, C., Electrical Conductivity and Magnetic Bistability in Metal-Organic Frameworks and Coordination Polymers: Charge Transport and Spin Crossover at the Nanoscale. *Chem. Soc. Rev.* 2020, 49 (15), 5601-5638.
- 4. (a) Stavila, V.; Talin, A. A.; Allendorf, M. D. MOF-based Electronic and Opto-Electronic Devices. Chem. Soc. Rev. 2014, 43, 5994-6010. (b) Ko, M.; Mendecki, L.; Mirica, K. A., Conductive Two-Dimensional Metal-Organic Frameworks as Multifunctional Materials. Chem. Commun. 2018, 54 (57), 7873-7891. (c) Wang, M.; Dong, R.; Feng, X., Two-Dimensional Conjugated Metal-Organic Frameworks (2D c-MOFs): Chemistry and Function for MOFtronics. Chem. Soc. Rev. 2021, 50 (4), 2764-2793. (d) Thorarinsdottir, A. E.; Harris, T. D. Metal-Organic Framework Magnets. Chem. Rev. 2020, 120, 8716-8789. (e) Huang, X.; Sheng, P.; Tu, Z.; Zhang, F.; Wang, J.; Geng, H.; Zou, Y.; Di, C.-a.; Yi, Y.; Sun, Y.; Xu, W.; Zhu, D., A twodimensional π-d conjugated coordination polymer with extremely high electrical conductivity and ambipolar transport behaviour. Nat. Commun. 2015, 6 (1), 7408. (f) Sun, L.; Liao, B.; Sheberla, D.; Kraemer, D.; Zhou, J.; Stach, E. A.; Zakharov, D.; Stavila, V.; Talin, A. A.; Ge, Y.; Allendorf, M. D.; Chen, G.; Léonard, F.; Dincă, M. A Microporous and Naturally Nanostructured Thermoelectric Metal-Organic Framework with Ultralow Thermal Conductivity. Joule 2017, 1, 168-177. (g) Feng, D.; Lei, T.; Lukatskaya, M. R.; Park, J.; Huang, Z.; Lee, M.; Shaw, L.; Chen, S.; Yakovenko, A. A.; Kulkarni, A.; Xiao, J.; Fredrickson, K.; Tok, J. B.; Zou, X.; Cui, Y.; Bao, Z., Robust and Conductive Two-Dimensional Metal-Organic Frameworks with Exceptionally High Volumetric and Areal Capacitance. Nat. Energy 2018, 3 (1), 30-36. (h) Arora, H.; Dong, R.; Venanzi, T.; Zscharschuch, J.; Schneider, H.; Helm, M.; Feng, X.; Cánovas, E.; Erbe, A., Demonstration of a Broadband Photodetector Based on a Two-Dimensional Metal-Organic Framework. Adv. Mater. 2020, 32 (9), 1907063.
- 5. (a) D'Alessandro, D. M., Exploiting Redox Activity in Metal-Organic Frameworks: Concepts, Trends and Perspectives. *Chem. Commun.* **2016**, *52* (58), 8957-8971. (b) Xie, L. S.; Skorupskii, G.; Dincă, M., Electrically Conductive Metal-Organic Frameworks. *Chem. Rev.* **2020**, *120* (16), 8536-8580. (c) Li, C.; Zhang, L.; Chen, J.; Li, X.; Sun, J.; Zhu, J.; Wang, X.; Fu, Y., Recent development and applications of electrical conductive MOFs. *Nanoscale* **2021**, *13* (2), 485-509. (d) Ahrenholtz, S. R.; Epley, C. C.; Morris, A. J., Solvothermal Preparation of an Electrocatalytic Metalloporphyrin

- MOF Thin Film and its Redox Hopping Charge-Transfer Mechanism. *J. Am. Chem. Soc.* **2014**, 136 (6), 2464-2472. (e) Duan, J.; Chen, S.; Zhao, C., Ultrathin metal-organic framework array for efficient electrocatalytic water splitting. *Nat. Commun.* **2017**, 8 (1), 15341.
- 6. (a) Darago, L. E.; Aubrey, M. L.; Yu, C. J.; Gonzalez, M. I.; Long, J. R., Electronic Conductivity, Ferrimagnetic Ordering, and Reductive Insertion Mediated by Organic Mixed-Valence in a Ferric Semiquinoid Metal-Organic Framework. J. Am. Chem. Soc. 2015, 137 (50), 15703-15711. (b) DeGayner, J. A.; Jeon, I.-R.; Sun, L.; Dincă, M.; Harris, T. D. 2D Conductive Iron-Quinoid Magnets Ordering up to Tc = 105 K via Heterogenous Redox Chemistry. J. Am. Chem. Soc. 2017, 139, (11), 4175-4184. (c) Aubrey, M. L.; Wiers, B. M.; Andrews, S. C.; Sakurai, T.; Reyes-Lillo, S. E.; Hamed, S. M.; Yu, C.-J.; Darago, L. E.; Mason, J. A.; Baeg, J.-O.; Grandjean, F.; Long, G. J.; Seki, S.; Neaton, J. B.; Yang, P.; Long, J. R., Electron Delocalization and Charge Mobility as a Function of Reduction in a Metal-Organic Framework. Nat. Mater. 2018, 17 (7), 625-632. (d) Wang, L.; Papoular, R. J.; Horwitz, N. E.; Xie, J.; Sarkar, A.; Campisi, D.; Zhao, N.; Cheng, B.; Grocke, G. L.; Ma, T.; Filatov, A. S.; Gagliardi, L.; Anderson, J. S., Linker Redox Mediated Control of Morphology and Properties in Semiconducting Iron-Semiquinoid Coordination Polymers. Angew. Chem. Int. Ed. 2022, 61 (45), e202207834.
- 7. (a) Wada, K.; Sakaushi, K.; Sasaki, S.; Nishihara, H., Multielectron-Transfer-based Rechargeable Energy Storage of Two-Dimensional Coordination Frameworks with Non-Innocent Ligands. *Angew. Chem. Int. Ed.* **2018,** 57 (29), 8886-8890. (b) Wu, Z.; Adekoya, D.; Huang, X.; Kiefel, M. J.; Xie, J.; Xu, W.; Zhang, Q.; Zhu, D.; Zhang, S., Highly Conductive Two-Dimensional Metal-Organic Frameworks for Resilient Lithium Storage with Superb Rate Capability. *ACS Nano* **2020,** 14 (9), 12016-12026. (c) Jiang, Q.; Xiong, P.; Liu, J.; Xie, Z.; Wang, Q.; Yang, X.-Q.; Hu, E.; Cao, Y.; Sun, J.; Xu, Y.; Chen, L., A Redox-Active 2D Metal-Organic Framework for Efficient Lithium Storage with Extraordinary High Capacity. *Angew. Chem. Int. Ed.* **2020,** 59 (13), 5273-5277.
- 8. (a) Contreras-Pereda, N.; Pané, S.; Puigmartí-Luis, J.; Ruiz-Molina, D., Conductive Properties of Triphenylene MOFs and COFs. Coord. Chem. Rev. 2022, 460, 214459. (b) Sheberla, D.; Sun, L.; Blood-Forsythe, M. A.; Er, S.; Wade, C. R.; Brozek, C. K.; Aspuru-Guzik, A.; Dincă, M., High Electrical Conductivity in Ni₃(2,3,6,7,10,11-hexaiminotriphenylene)2, a Semiconducting Metal–Organic Graphene Analogue. J. Am. Chem. Soc. 2014, 136 (25), 8859-8862. (c) Sun, L.; Yang, L.; Dou, J.-H.; Li, J.; Skorupskii, G.; Mardini, M.; Tan, K. O.; Chen, T.; Sun, C.; Oppenheim, J. J.; Griffin, R. G.; Dincă, M.; Rajh, T., Room-Temperature Quantitative Quantum Sensing of Lithium Ions with a Radical-Embedded Metal–Organic Framework. J. Am. Chem. Soc. 2022, 144 (41), 19008-19016. (d) Stodolka, M.; Choi, J. Y.; Flood, J.; Pham, H. T. B.; Park, J., Iron-Based 2D Conductive Metal–Organic Framework Nanostructure with Enhanced Pseudocapacitance. ACS Appl. Nano Mater. 2022, 5 (2), 2156-2162.
- 9. (a) Mendecki, L.; Ko, M.; Zhang, X.; Meng, Z.; Mirica, K. A., Porous Scaffolds for Electrochemically Controlled Reversible Capture and Release of Ethylene. *J. Am. Chem. Soc.* **2017**, *139* (48), 17229-17232. (b) Clough, A. J.; Skelton, J. M.; Downes, C. A.; de la Rosa, A. A.; Yoo, J. W.; Walsh, A.; Melot, B. C.; Marinescu, S. C., Metallic Conductivity in a Two-Dimensional Cobalt Dithiolene Metal–Organic Framework. *J. Am. Chem. Soc.* **2017**, *139* (31), 10863-10867. (c) Dong, R.; Han, P.; Arora, H.; Ballabio, M.; Karakus, M.; Zhang, Z.; Shekhar, C.; Adler, P.; Petkov, P. S.; Erbe, A.; Mannsfeld, S. C. B.; Felser, C.; Heine, T.; Bonn, M.; Feng, X.; Cánovas, E., High-mobility Band-Like Charge Transport in a Semiconducting Two-Dimensional Metal–Organic Framework. *Nat. Mater.* **2018**, *17* (11), 1027-1032. (d) Clough, A. J.; Orchanian, N. M.; Skelton, J. M.; Neer, A. J.; Howard, S. A.; Downes, C. A.; Piper, L. F. J.; Walsh, A.; Melot, B. C.; Marinescu, S. C., Room Temperature Metallic Conductivity in a Metal–Organic Framework Induced by Oxidation. *J. Am. Chem. Soc.* **2019**, *141* (41), 16323-16330.
- 10. Pal, T.; Doi, S.; Maeda, H.; Wada, K.; Tan, C. M.; Fukui, N.; Sakamoto, R.; Tsuneyuki, S.; Sasaki, S.; Nishihara, H., Interfacial Transmetallation Synthesis of a Platinadithiolene Nanosheet as a Potential 2D Topological Insulator. *Chem. Sci.* **2019**, *10* (20), 5218-5225.

- 11. (a) Howarth, A. J.; Peters, A. W.; Vermeulen, N. A.; Wang, T. C.; Hupp, J. T.; Farha, O. K., Best Practices for the Synthesis, Activation, and Characterization of Metal–Organic Frameworks. *Chem. Mater.* **2017**, *29* (1), 26-39. (b) Forgan, R. S., Modulated Self-Assembly of Metal–Organic Frameworks. *Chem. Sci.* **2020**, *11* (18), 4546-4562.
- 12. (a) Jia, Q.; Ramaswamy, N.; Hafiz, H.; Tylus, U.; Strickland, K.; Wu, G.; Barbiellini, B.; Bansil, A.; Holby, E. F.; Zelenay, P.; Mukerjee, S., Experimental Observation of Redox-Induced Fe–N Switching Behavior as a Determinant Role for Oxygen Reduction Activity. ACS Nano 2015, 9 (12), 12496-12505. (b) Jia, Q.; Liu, E.; Jiao, L.; Pann, S.; Mukerjee, S., X-Ray Absorption Spectroscopy Characterizations on PGM-Free Electrocatalysts: Justification, Advantages, and Limitations. Adv. Mater. 2019, 31 (31), 1805157. (c) Dong, R.; Zhang, Z.; Tranca, D. C.; Zhou, S.; Wang, M.; Adler, P.; Liao, Z.; Liu, F.; Sun, Y.; Shi, W.; Zhang, Z.; Zschech, E.; Mannsfeld, S. C. B.; Felser, C.; Feng, X., A coronene-based Semiconducting Two-Dimensional Metal-Organic Framework with Ferromagnetic Behavior. Nat. Commun. 2018, 9 (1), 2637.
- 13. (a) Sproules, S.; Wieghardt, K., o-Dithiolene and o-aminothiolate chemistry of iron: Synthesis, Structure and Reactivity. *Coord. Chem. Rev.* **2010**, 254 (13), 1358-1382. (b) Eisenberg, R.; Gray, H. B., Noninnocence in Metal Complexes: A Dithiolene Dawn. *Inorg. Chem.* **2011**, 50 (20), 9741-9751. (c) Patra, A. K.; Bill, E.; Weyhermüller, T.; Stobie, K.; Bell, Z.; Ward, M. D.; McCleverty, J. A.; Wieghardt, K., Dinuclear Bis(1,2-diaryl-1,2-ethylenedithiolato)iron Complexes: $[Fe^{III}_2(L)_4]n$ (n = 2-, 1-, 0, 1+). *Inorg. Chem.* **2006**, 45 (16), 6541-6548.
- 14. (a) Auerbach, H.; Giammanco, G. E.; Schünemann, V.; Ostrowski, A. D.; Carrano, C. J., Mössbauer Spectroscopic Characterization of Iron(III)—Polysaccharide Coordination Complexes: Photochemistry, Biological, and Photoresponsive Materials Implications. *Inorg. Chem.* 2017, 56 (19), 11524-11531. (b) DeGayner, J. A.; Wang, K.; Harris, T. D., A Ferric Semiquinoid Single-Chain Magnet via Thermally-Switchable Metal–Ligand Electron Transfer. *J. Am. Chem. Soc.* 2018, 140 (21), 6550-6553.
- 15. (a) Rao, C.; Venkataraghavan, R.; Kasturi, T., Contribution to the infrared spectra of organosulphur compounds. *Can. J. Chem.* **1964**, 42 (1), 36-42. (b) Wang, X.; Zhang, Z.; Yan, X.; Qu, Y.; Lai, Y.; Li, J., Interface Polymerization Synthesis of Conductive Polymer/Graphite Oxide@Sulfur Composites for High-Rate Lithium-Sulfur Batteries. *Electrochim. Acta* **2015**, 155, 54-60.
- 16. Ziebel, M. E.; Darago, L. E.; Long, J. R., Control of Electronic Structure and Conductivity in Two-Dimensional Metal–Semiquinoid Frameworks of Titanium, Vanadium, and Chromium. *J. Am. Chem. Soc.* **2018**, *140* (8), 3040-3051.
- 17. (a) Lin, T. T.; Young, S. L.; Kung, C. Y.; Chen, H. Z.; Kao, M. C.; Chang, M. C.; Ou, C. R., Variable-Range Hopping and Thermal Activation Conduction of Y-Doped ZnO Nanocrystalline Films. *IEEE Trans Nanotechnol* **2014**, *1*3 (3), 425-430. (b) Halim, J.; Moon, E. J.; Eklund, P.; Rosen, J.; Barsoum, M. W.; Ouisse, T., Variable Range Hopping and Thermally Activated Transport in Molybdenum-Based MXenes. *Phys. Rev. B* **2018**, *98* (10), 104202.
- 18. Qiu, H.; Xu, T.; Wang, Z.; Ren, W.; Nan, H.; Ni, Z.; Chen, Q.; Yuan, S.; Miao, F.; Song, F.; Long, G.; Shi, Y.; Sun, L.; Wang, J.; Wang, X., Hopping Transport Through Defect-Induced Localized States in Molybdenum Disulphide. *Nat. Commun.* **2013**, *4* (1), 2642.
- 19. Sun, L.; Hendon, C. H.; Park, S. S.; Tulchinsky, Y.; Wan, R.; Wang, F.; Walsh, A.; Dincă, M., Is Iron Unique in Promoting Electrical Conductivity in MOFs? *Chem. Sci.* **2017**, *8* (6), 4450-4457.
- 20. (a) Gurlo, A.; Bârsan, N.; Oprea, A.; Sahm, M.; Sahm, T.; Weimar, U., An n- to p-type Conductivity Transition Induced by Oxygen Adsorption on α-Fe₂O₃. *Appl. Phys. Lett.* **2004**, *85* (12), 2280-2282. (b) He, Q.; Liu, Y.; Tan, C.; Zhai, W.; Nam, G.-h.; Zhang, H., Quest for p-Type Two-Dimensional Semiconductors. *ACS Nano* **2019**, *13* (11), 12294-12300. (c) Wen, T.; Wang, Y.; Li, N.; Zhang, Q.; Zhao, Y.; Yang, W.; Zhao, Y.; Mao, H.-k., Pressure-Driven Reversible Switching between n- and p-Type Conduction in Chalcopyrite CuFeS₂. *J. Am. Chem. Soc.* **2019**, *141* (1), 505-510. (d) Xie, J.; Pan, J.-A.; Cheng, B.; Ma, T.; Filatov, A. S.; Patel, S. N.; Park, J.; Talapin,

- D. V.; Anderson, J. S., Presynthetic Redox Gated Metal-to-Insulator Transition and Photothermoelectric Properties in Nickel Tetrathiafulvalene-Tetrathiolate Coordination Polymers. *J. Am. Chem. Soc.* **2022**, *144* (41), 19026-19037.
- 21. Redel, E.; Baumgart, H., Thermoelectric Porous MOF Based Hybrid Materials. *APL Mater.* **2020**, *8* (6), 060902.
- Wood, C., Materials for Thermoelectric Energy Conversion. Rep. Prog. Phys. 1988, 51 (4), 459-539.
- 23. Perdew, J. P.; Ruzsinszky, A.; Csonka, G. I.; Vydrov, O. A.; Scuseria, G. E.; Constantin, L. A.; Zhou, X.; Burke, K., Restoring the Density-Gradient Expansion for Exchange in Solids and Surfaces. *Phys. Rev. Lett.* **2008**, *100* (13), 136406.
- 24. (a) Choudhuri, I.; Truhlar, D. G., Improved Predictive Tools for Structural Properties of Metal-Organic Frameworks. *Molecules* **2020**, *25* (7), 1552. (b) Chen, K.; Downes, C. A.; Schneider, E.; Goodpaster, J. D.; Marinescu, S. C., Improving and Understanding the Hydrogen Evolving Activity of a Cobalt Dithiolene Metal-Organic Framework. *ACS Appl. Mater. Interfaces* **2021**, *13* (14), 16384-16395.
- 25. (a) Grimme, S.; Ehrlich, S.; Goerigk, L., Effect of the damping function in dispersion corrected density functional theory. *J. Comput. Chem.* **2011**, 32 (7), 1456-1465. (b) Grimme, S.; Antony, J.; Ehrlich, S.; Krieg, H., A Consistent and Accurate Ab Initio Parametrization of Density Functional Dispersion Correction (DFT-D) for the 94 Elements H-Pu. *J. Chem. Phys.* **2010**, 132 (15), 154104.
- 26. (a) Kresse, G.; Hafner, J., Ab Initio Molecular Dynamics for Open-Shell Transition Metals. *Phys. Rev. B* **1993**, *48* (17), 13115-13118. (b) Kresse, G.; Hafner, J., Norm-Conserving and Ultrasoft Pseudopotentials for First-Row and transition elements. *J. Phys. Condens. Matter* **1994**, *6* (40), 8245. (c) Kresse, G.; Furthmüller, J., Efficiency of Ab-Initio Total Energy Calculations for Metals and Semiconductors Using a Plane-Wave Basis Set. *Comput. Mater. Sci.* **1996**, *6* (1), 15-50.
- 27. Kulik, H. J.; Cococcioni, M.; Scherlis, D. A.; Marzari, N., Density Functional Theory in Transition-Metal Chemistry: A Self-Consistent Hubbard *U* Approach. *Phys. Rev. Lett.* **2006**, *97* (10), 103001.
- 28. Misumi, Y.; Yamaguchi, A.; Zhang, Z.; Matsushita, T.; Wada, N.; Tsuchiizu, M.; Awaga, K., Quantum Spin Liquid State in a Two-Dimensional Semiconductive Metal—Organic Framework. *J. Am. Chem. Soc.* **2020**, 142 (39), 16513-16517.
- 29. Toby, B. H.; Von Dreele, R. B., GSAS-II: the Genesis of a Modern Open-Source All Purpose Crystallography Software Package. *J. Appl. Cryst.* **2013**, *46* (2), 544-549.
- 30. Morrison, C.; Sun, H.; Yao, Y.; Loomis, R. A.; Buhro, W. E., Methods for the ICP-OES Analysis of Semiconductor Materials. *Chem. Mater.* **2020**, 32 (5), 1760-1768.
- 31. Ma, T.; Dong, B. X.; Grocke, G. L.; Strzalka, J.; Patel, S. N. Leveraging Sequential Doping of Semiconducting Polymers to Enable Functionally Graded Materials for Organic Thermoelectrics. *Macromolecules* **2020**, *53* (8), 2882-2892.
- 32. Reenen, S. v.; Kemerink, M., Correcting for Contact Geometry in Seebeck Coefficient Measurements of Thin Film Devices. *Org. Electron.* **2014**, *15* (10), 2250-2255.
- 33. Jang, J.; Liu, W.; Son, J. S.; Talapin, D. V., Temperature-Dependent Hall and Field-Effect Mobility in Strongly Coupled All-Inorganic Nanocrystal Arrays. *Nano Lett.* **2014**, *14* (2), 653-662.
- 34. Kresse, G.; Joubert, D., From Ultrasoft Pseudopotentials to the Projector Augmented-Wave Method. *Phys. Rev. B* **1999**, *59* (3), 1758-1775.
- 35. Grimme, S.; Ehrlich, S.; Goerigk, L., Effect of the Damping Function in Dispersion Corrected Density Functional Theory. *J. Comput. Chem.* **2011**, 32 (7), 1456-1465.
- 36. Pack, J. D.; Monkhorst, H. J., "Special Points for Brillouin-Zone Integrations"---a reply. *Phys. Rev. B* **1977**, *16* (4), 1748-1749.

